JGR Space Physics

TECHNICAL REPORTS: DATA

10.1029/2019JA027487

Special Section:
Early results from the Global-scale Observations of the Limb and Disk (GOLD) mission

Early Morning Equatorial Ionization Anomaly From GOLD Observations

F. I. Laskar[1], R. W. Eastes[1], C. R. Martinis[2], R. E. Daniell[3], N. M. Pedatella[4], A. G. Burns[4], W. McClintock[1], L. P. Goncharenko[5], A. Coster[5], M. A. Milla[6], W. Wang[4], C. E. Valladares[7], and M. V. Codrescu[8]

[1]Laboratory for Atmospheric and Space Physics, University of Colorado, Bouder, CO, USA, [2]Center for Space Physics, Boston University, Boston, MA, USA, [3]Ionospheric Physics Consulting, Stoughton, MA, USA , [4]High Altitude Observatory, National Center for Atmospheric Research, Boulder, CO, USA, [5]MIT Haystack Observatory, Westford, MA, USA, [6]Jicamarca Radio Observatory, Lima, Peru, [7]William B Hanson Center for Space Sciences, University of Texas Dallas, Dallas, TX, USA, [8]Space Weather Prediction Center, NOAA, Boulder, CO, USA

Abstract During geomagnetically quiet and solar minimum conditions, spatial variations of the early morning thermosphere-ionosphere (TI) system are expected to be mainly governed by wave dynamics. To study the postmidnight dynamical coupling, we investigated the early morning equatorial ionization anomaly (EIA) using Global-scale Observations of the Limb and Disk (GOLD) measurements of OI-135.6 nm nightglow emission and global navigation satellite system (GNSS)-based total electron content (TEC) maps. The EIA structures in the OI-135.6 nm emission over the American landmass resemble, spatially and temporally, those observed in the GNSS-TEC maps. The early morning EIA (EM-EIA) crests are well separated in latitude and mostly located over the middle of South America during October–November. In February–April the crests are less separated in latitude and predominantly located over the west coast sector of South America. Whole Atmosphere Community Climate Model with thermosphere and ionosphere eXtension (WACCMX) simulations with constant solar minimum and quiet-geomagnetic conditions show that EM-EIA can occur globally and shows properties similar to longitudinal Wave 4 pattern. Thus, we propose that EM-EIA is driven by dynamical changes associated with the lower atmospheric waves.

Key Points:
- GOLD observes early morning EIA in OI-135.6 nm airglow over South America
- Radiative recombination is the predominant mechanism giving rise to the early morning emissions in the EIA region
- WACCMX simulations show that early morning EIA can occur globally and has properties similar to longitudinal Wave 4 structure

Supporting Information:
- Supporting Information S1

Correspondence to:
F. I. Laskar,
Fazlul.Laskar@colorado.edu

Citation:
Laskar, F. I., Eastes, R. W., Martinis, C. R., Daniell, R. E., Pedatella, N. M., Burns, A. G., et al. (2020). Early morning equatorial ionization anomaly from GOLD observations. *Journal of Geophysical Research: Space Physics*, *125*, e2019JA027487. https://doi.org/10.1029/2019JA027487

Received 3 OCT 2019
Accepted 13 MAY 2020
Accepted article online 21 MAY 2020

1. Introduction

The thermosphere-ionosphere (TI) system of the Earth is influenced by solar, magnetospheric, geomagnetic, and lower atmospheric forcings. For a better understanding of the TI variability, it is important to investigate the role of each process. The postmidnight to presunrise time sector during quiet geomagnetic conditions is ideal, as the TI variability in these hours will not be influenced by solar forcings. Although in the postmidnight sector the ionospheric plasma bubbles are mostly weak (Heelis et al., 2010; Su et al., 2006), there are several reports of their occurrences (Heelis et al., 2010; Patra & Phanikumar, 2009; Rodrigues et al., 2018; Sekar et al., 2007; Yizengaw et al., 2013), suggesting that the postmidnight ionosphere is not simply a remnant from earlier hours (McDonald et al., 2008) but can be very dynamic. Though the neutral composition and thermal profile will be influenced by solar activity by changing the background ionospheric conditions, the longitudinal variability will be mainly governed by dynamics (Immel et al., 2006) and magnetic field configuration (Zhang et al., 2018).

The equatorial ionization anomaly (EIA) has been known for more than half a century (Appleton, 1946). It occurs in the equatorial ionosphere due to generation of an eastward electric field (E) perpendicular to magnetic field (B) by westward zonal wind. $E \times B$ drift of the charged particles lifts plasma up in the F region over the equator, which then under the combined action of gravity and pressure gradient forces diffuse away from the equator along the magnetic field to produce the EIA (e.g., Rishbeth, 1997). Depending on local and global dynamical and electrodynamical conditions, the EIA can have varied latitudinal and longitudinal variability. As the waves from lower atmosphere can propagate to the TI system, they can affect the E and F region electric fields to influence the EIA generation and evolution (Rishbeth, 1997).

It is well recognized that in general the most prominent variability in the low-latitude TI is due to tides, either generated in situ or propagating from below (Laskar et al., 2014; Liu, 2016; Liu & Richmond, 2013).

The in situ tides are generally driven by solar forcing, and thus, they migrate with the Sun. Tides originating in the lower atmosphere (troposphere and stratosphere) could propagate to the TI system and thus produce secondary variations. While propagating up in the atmosphere, their amplitudes grow; thus, they play a role in the TI variability (Laskar et al., 2013; Yamazaki & Richmond, 2013). Even though many of these waves reach maximum amplitudes in the lower thermosphere and dissipate at higher altitudes, they can also influence the filtering of other shorter-period waves, such as gravity waves (GWs) propagating from below, and alter the ambient state of the TI system. Other than those, migrating and nonmigrating tides from lower atmosphere can also influence the TI system. For example, the longitudinal Wave 4 structure observed in ionospheric and neutral atmospheric parameters in the TI is primarily attributed to the diurnal eastward propagating Wave Number 3 (DE3) nonmigrating tide (England et al., 2006; Immel et al., 2006), though they can also be generated by semidiurnal eastward propagating nonmigrating tide with zonal Wave Number 2 (SE2) and stationary planetary wave of Wave Number 4 (SPW4) (Chang et al., 2013; Pedatella et al., 2012).

As demonstrated by Dao et al. (2011), the daytime vertical drifts can strongly affect nighttime ambient electron density in the low-latitude *F* region. Dao et al. (2011) have clearly demonstrated this possibility for solar minimum conditions. They used a global ionospheric model described by Retterer (2005) to investigate sensitivity of the midnight ionospheric electron density to the strength of daytime vertical drifts and concluded that increasing daytime (6–18 local time [LT]) vertical drift by 10 m/s results in a significant increase in electron density at night.

Local electron density enhancements in the postmidnight sector were reported in the past using Global Positioning System (GPS) and low-Earth orbiting satellite-based electron density measurements (Liu et al., 2011; McDonald et al., 2008; Yizengaw et al., 2009). For example, Yizengaw et al. (2009) found that in addition to the remnant plasma from the premidnight sector, the postmidnight EIA can arise from a fresh lifting-up of plasma by upward *F* region drifts in the postmidnight sector. Also, Batista et al. (2006) reported a case of EM-EIA intensification in response to highly dynamic meridional wind disturbance generated by an intense geomagnetic storm. The above studies were during high solar activity when the background density and plasma are much higher compared to low-solar activity conditions. Also, the GPS-based studies were possible only over the continents, as there are no GPS receivers overt the Oceans. In the present study, we investigate the early morning EIA (EM-EIA) during quiet-time low solar activity and with the newly available Global-scale Observations of the Limb and Disk (GOLD) satellite-based oxygen emissions that are measured at unprecedented spatial resolution and coverage, extending from Pacific to Atlantic Oceans. The main objective of this study is to investigate the properties of postmidnight EIA development in a synoptic scale over the Americas and to discuss the role of lower atmospheric waves.

This paper is organized as follows. In section 2 data and analysis methodology are described. Section 3 presents results, which are discussed in section 4. Finally, in section 5 we present the conclusions arrived from results presented in this paper.

2. Data and Analysis Methodology

The primary data used for this investigation are from GOLD early morning OI-135.6 nm emission intensities, which are augmented by global navigation satellite system (GNSS)-based total electron content (TEC) maps. This section describes the technical details of each of these data sets.

2.1. GOLD

The GOLD imager is a payload on the SES-14 (Société Européenne des Satellites-14) satellite in geostationary orbit whose subsatellite point is at 47.5° W and over the equator. It observes the Earth's limb and disk for about 18 hr each day, covering various solar LTs over the Americas. GOLD has two independent, identical imaging spectrographs covering 132–162 nm at a spectral resolution of about 0.2 nm. The spatial grid at ionospheric altitudes is binned to 125 × 125 km for day scans, but the intrinsic resolution is about 50 km. The Channel A observations are mainly for the day-disk scans, and Channel B is dedicated primarily to nighttime observations. The first hour of Channel A disk observations use a low-resolution slit as majority of the disk covers the night side during this hour. The low-resolution slit observations use a wider slit to allow more light to enter through the slit, so they are able to make observations even on the night side. To avoid direct sunlight, GOLD is not being operated from about 0030 to 0610 UT hours (Eastes et al., 2017). So the first scan of any day starts at 0610 UT. Further technical details about the GOLD instrument, operation schedules, and observations can be found in Eastes et al. (2017, 2019).

2.2. GNSS Total Electron Content

The TEC data sets used in this study are from worldwide GNSS ground-based receivers. Using time delay of received radio signals from the GNSS satellites, the line-of-sight integrated electron content is derived, which are then mapped to vertical TEC. The vertical TEC data are subsequently binned in 5 min temporal and 1° by 1° spatial bins. The TEC data are available at the CEDAR Madrigal database (https://cedar.openmadrigal.org). The TEC retrieval algorithm was originally developed by Rideout and Coster (2006) and has been improved by Vierinen et al. (2016). In the current study the TEC maps are hourly averages to compare them with the GOLD hourly averaged OI-135.6 nm disk images.

2.3. Whole Atmosphere Community Climate Model With Thermosphere-Ionosphere eXtension

The recently developed Whole Atmosphere Community Climate Model with thermosphere-ionosphere eXtension (WACCMX) Version 2.1 is a whole atmosphere general circulation model extending from the surface to the upper thermosphere (~500–700 km depending on solar activity) (Liu et al., 2018). WACCMX includes the chemical, dynamical, and physical processes that are necessary to model the lower, middle, and upper atmospheres. The thermosphere and ionosphere processes calculated are similar to those in the NCAR Thermosphere-Ionosphere-Electrodynamics General Circulation Model (TIE-GCM), including the transport of O^+ and self-consistent electrodynamics as well as realistic solar and geomagnetic forcing. The model horizontal resolution is 1.9° × 2.5° in latitude and longitude, and the vertical resolution is 0.25 scale heights above ~50 km. For the current study WACCMX simulations are performed for solar minimum (with F10.7 flux of 70 sfu; 1 sfu = 10^{-22} W m^{-2} Hz^{-1}) and geomagnetically quiet (with ap = 4 and kp = 1) conditions. It may be noted here that WACCMX has a self-consistent lower atmospheric weather that can produce various forcing conditions that change with season. As this is a free-running simulation, it is not a representative of any real year in the lower atmosphere.

3. Results

Figure 1 shows hourly averaged GOLD early morning disk observations during six representative days from October 2018 and March–April 2019. Each image shown in Figure 1 is an average of two "Level 1C - Day" scans of the full disk, which takes about an hour. The start and end times of Northern Hemisphere 6–7 UT hour scan cycles are 0610–0622 and 0640–0652 UT and of Southern Hemisphere scans are 0622–0640 and 0652–0704 UT. The LT corresponding to the center of the image, that is, at the subsatellite point for the 6–7 UT, is about 3–4 LT. The image averaging was performed to achieve better signal-to-noise ratio (SNR), as the signal integration time of the disk scans is optimized for the strong signals occurring during daylight hours. The random errors vary with radiation belt noise but are, in general, below 5 Rayleigh (R), 1 R = $(1/4\pi) \times 10^{10}$ photons m^{-2} s^{-1} sr^{-1}. To investigate the seasonal climatology of EM-EIA, the monthly mean GOLD disk scans during 6–7 UT are presented in Figure 2.

Salient features that are observed in plots similar to Figure 1 and in Figure 2 for the 10 months (October 2018 to July 2019) of GOLD nighttime observations are as follows: (i) in the Northern Fall (October–November), the EM-EIA is mostly over central South America (2–4 LT sector, i.e., closer to the solar terminator), whereas during the Northern Spring (March–April), it is over the western coast of South America (about 1–3 LT sector); (ii) in Northern winter and summer months, there is no EM-EIA (as can be seen in Figure 2); and (iii) typical values of OI-135.6 nm emissions at the EM-EIA crest are in the range 5–15 R.

As the Channel A observations are configured for day scans, the GOLD disk observations on the night side are noisy even after averaging two scans. GOLD has another independent spectrograph, Channel B, which can make coincident, higher SNR nighttime observations by using its low-resolution slit. Such early morning night-side observations began on 18 March 2019. Figure 3 shows the Channel B observations on 19 March and 15 April, which can be compared with the Channel A observations on these dates in Figures 1e and 1f. The EM-EIA structures are better defined in Figure 3. The Channel B observations compare well with the corresponding Channel A observations in Figures 1e and 1f, but with better SNR, thus confirming that the EM-EIA structures seen in the disk scans are indeed real geophysical features of the TI system. It may be noted that there are two sets of scans during 6–7 UT that are alternately in the eastern and western (over Pacific ocean) sectors as can be seen in Figure 3. The western and eastern scans start at 0610 and 0640 UT, respectively, and each of them last for about 12 min.

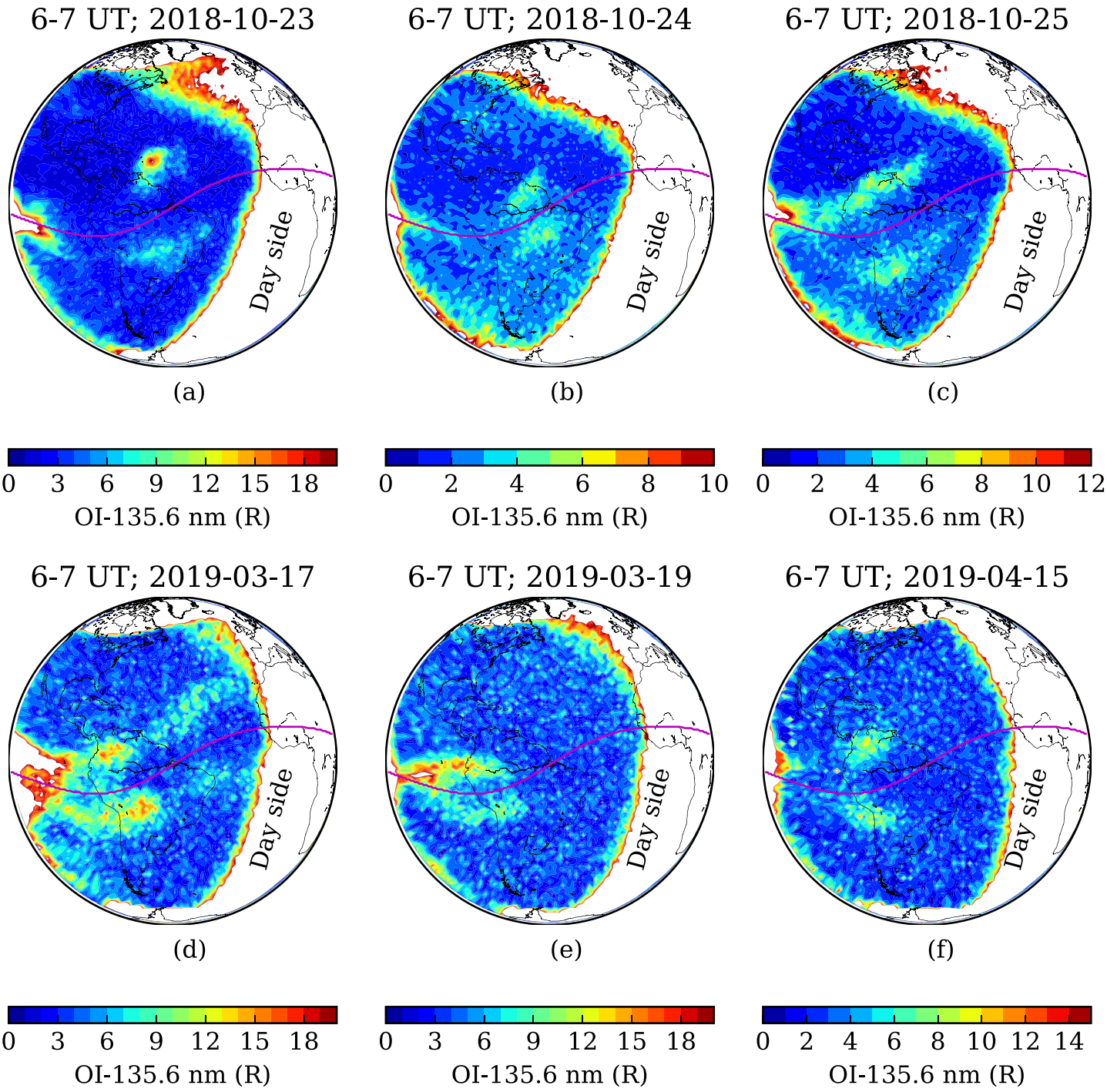

Figure 1. Example early morning localized EIA observed by GOLD early morning disk scans on some representative days during October 2018 and March–April of 2019. Each whole disk image is a composite of four images, two in each hemisphere obtained during regular Channel A scans during 6 to 7 hr universal time (6–7 UT).

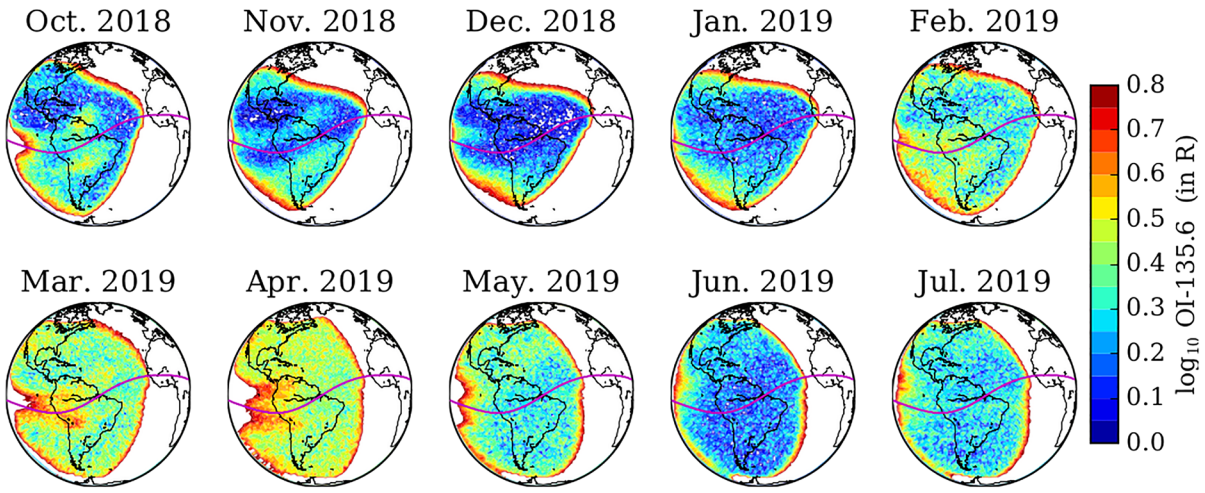

Figure 2. A monthly composite of the hourly averaged GOLD OI-135.6 nm disk observations is used to see the seasonal evolution of the EM-EIA. It can be seen that they are mostly present during fall and spring season in the GOLD field of view.

4. Discussion

4.1. Why EM-EIA Is Seen in GOLD OI-135.6 nm Emission

To understand why the EM-EIA is observed by GOLD, it is necessary to first explain the production mechanism of the nighttime OI-135.6 nm emissions. In the nighttime thermosphere the OI-135.6 nm emission is mainly produced by radiative recombination of $O^+ + e^- \rightarrow O + h\nu_{135.6}$, where h is Plank's constant and $\nu_{135.6}$ is for OI-135.6 nm photon (Meléndez-Alvira et al., 1999; Qin et al., 2015). Another mechanism that produces a smaller amount of OI-135.6 nm emission is from the mutual neutralization chemistry of the $O^+ + O^- \rightarrow O + O^*$, where O^* is the excited $O(^5S_2)$ state which de-excites to $O(^3P_{2,1})$ to produce the emission (Hanson, 1970; Meléndez-Alvira et al., 1999; Qin et al., 2015; Tinsley et al., 1973).

To investigate the role of radiative recombination process, we compare the GOLD EM-EIA emissions with GNSS-TEC measurements over American longitudes. Figure 4 shows a comparison for the 23 October 2018 EM-EIA case. In this figure, 6–7 UT average (mean of the hour during 0610–0704 UT) TEC and OI-135.6

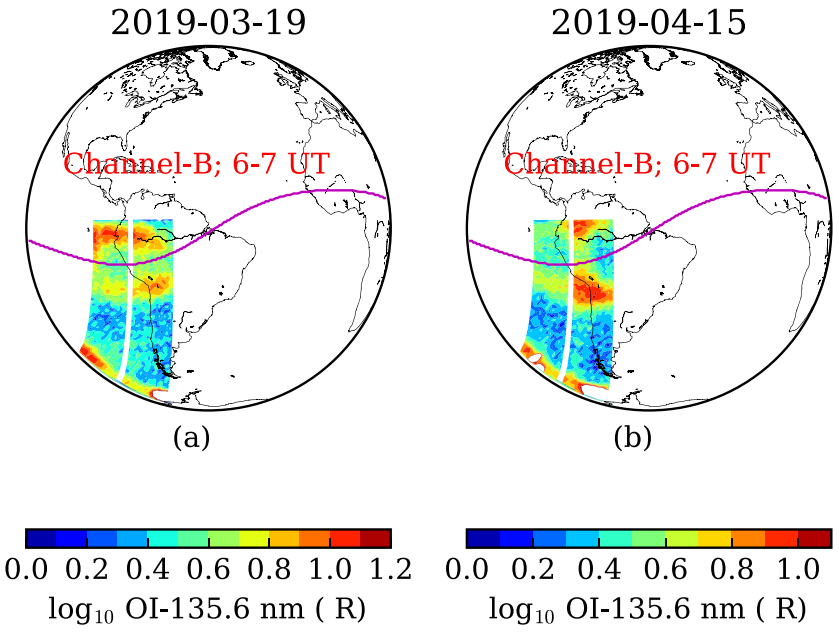

Figure 3. GOLD Channel B observations of the EM-EIA for 19 March and 15 April 2019. The Channel B observations have high SNR compared to the Channel A daytime disk observations shown in Figures 1e and 1f.

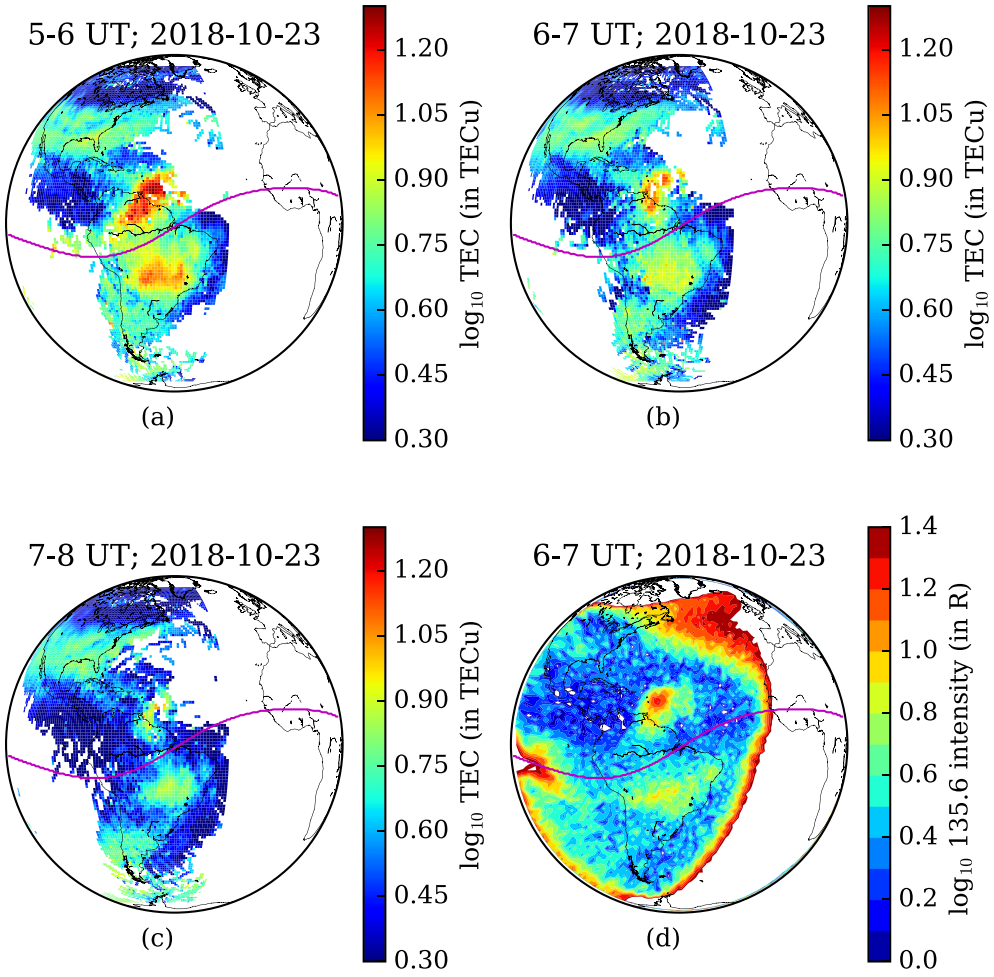

Figure 4. Comparison of hourly averaged GNSS TEC for 23 October 2018 with GOLD OI-135.6 nm emissions on that day (in d). One can see remarkable agreement between EIA structures in TEC (in b) and in GOLD OI-135.6 nm emission (in d). Other than 6–7 UT TEC, an hour before (5-6 UT) and after (7-8 UT) is also shown in (a) and (c), to see continuity of the ionospheric anomalous feature.

nm emissions are shown in (b) and (d), respectively. TEC observations for an hour before (5–6 UT, in a) and an hour after (7–8 UT, in c) the GOLD early morning observation (in d) are also shown for investigation of possible spatiotemporal connections. From this comparison it is clear that the majority of the structures in the equatorial region compare very well between airglow and TEC. But GOLD can provide a more complete picture of the EIA, including some regions over the Atlantic and Pacific Oceans, which is not possible using GNSS TEC. For example, the localized EIA crest structure in the Northern Hemisphere in GOLD observations (Figure 4d) cannot be unambiguously identified from TEC in Figure 4b or in Figures 4a and 4c. In other words, from TEC observations alone one cannot say that the Northern EIA-crest structure is localized or extended in longitude. But from GOLD observations it is clear that this is a very localized structure. But over the landmass, clear conformity between airglow and TEC is observed (not shown here) for all the days in Figure 1. This agreement confirms that radiative recombination is the dominant process for the production of the OI-135.6 nm nightglow. The remarkable agreement between GOLD OI-135.6 nm emissions and GNSS TEC measurements provides an unambiguous experimental validation of the GOLD early morning and thus nighttime observations. So such data can be used for the studies of the nighttime ionospheric dynamics and plasma bubble investigations. Another striking feature is that the strongest EIA structures are very localized over South America.

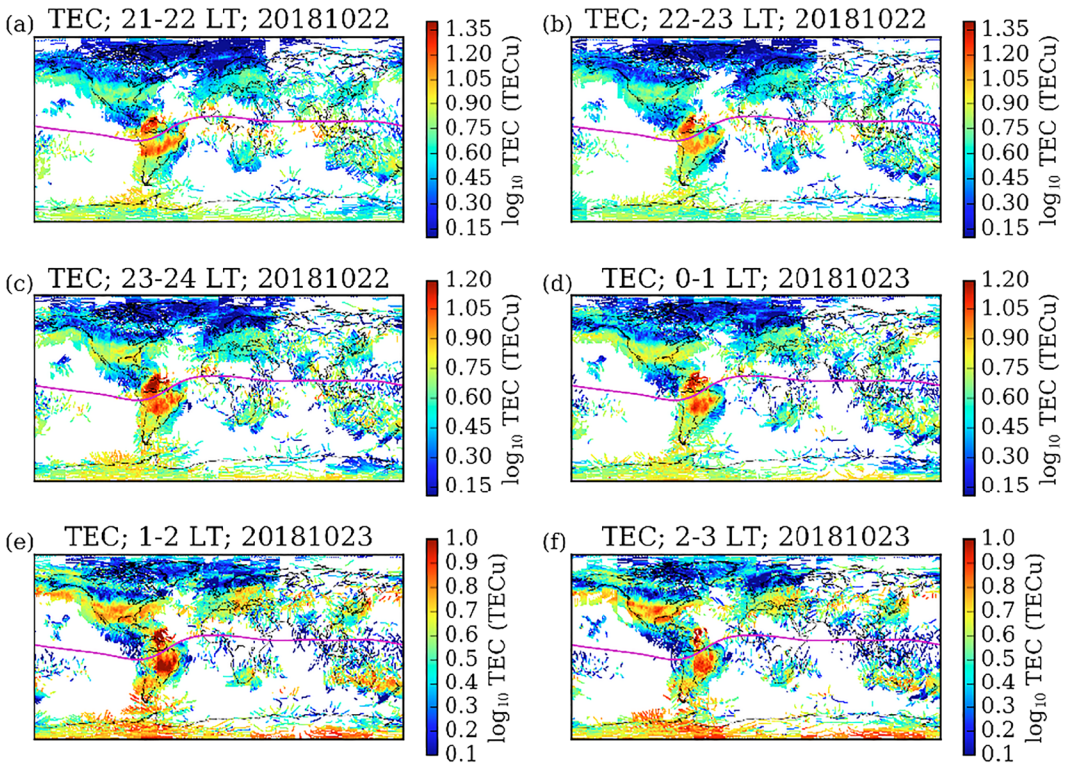

Figure 5. Global TEC from GNSS receivers at different local times on 22 and 23 October 2018. It can be seen that there is a unique region of enhanced TEC over the middle of South America, which remains persistent even in early morning sector (2–3 LT).

4.2. Spatial and Temporal Variability of EM-EIA

In Figures 1–4 the strongest EM-EIA structures are located over South America as observed by GOLD. To demonstrate the presence of similar EM-EIA structures, if they occur, at other longitude sectors we would ideally need three additional GOLD-like instruments over the Pacific, Indian, and Atlantic oceans. In the absence of such observations, multiyear seasonal averaged satellite observations may provide useful information about the presence of EM-EIA in other longitude sectors. Though such data are not available during GOLD observation years, investigations using past Constellation Observing System for Meteorology, Ionosphere, and Climate (COSMIC) data are available in the literature (e.g., Zhong et al., 2019). For example, Figures 2, 3e and 3h of Zhong et al. (2019) show that there are four longitudinal maxima in postmidnight equatorial COSMIC electron densities during September and March equinoxes at low solar activity conditions with F10.7 < 75 sfu. It can also be noted from their figures that one of the maxima occurs over South America, where GOLD also sees EM-EIA in the same seasons but for a different year. But the development and separation of two EIA crests were not seen in COSMIC data, which could be due to poor latitudinal resolution and multiyear averages for the COSMIC observations. The spatial variations with Wave 4 structure as seen in the COSMIC observations do, however, suggest that the EM-EIA may occur in other longitude sectors.

It is known that low-Earth orbit satellite data are not adequate for studies of temporal evolution with high resolution. Fortunately, the GNSS TEC data over Americas have very good temporal and spatial coverage, so they can be used to study the temporal evolution of the EIA during the premidnight and postmidnight hours. Figure 5 shows the LT evolution of the global GNSS TEC at hourly intervals from 21 LT on 22 October to 3 LT on 23 October 2018. As the dominant EIA structures are seen to have spatial similarity between the premidnight and postmidnight sectors, it can be stated that the EM-EIA is the remnant of premidnight sector plasma, which spreads along magnetic field lines under the action of gravity and pressure gradient forces. But due to gaps in TEC data, it is not possible to see if similar localized EM-EIA occurs in TEC over, for example, Africa, Asia, or the Pacific Ocean. However, from the GOLD observations in Figure 4, which also provide information over part of the Pacific and Atlantic Oceans, it can be seen that the EM-EIA over

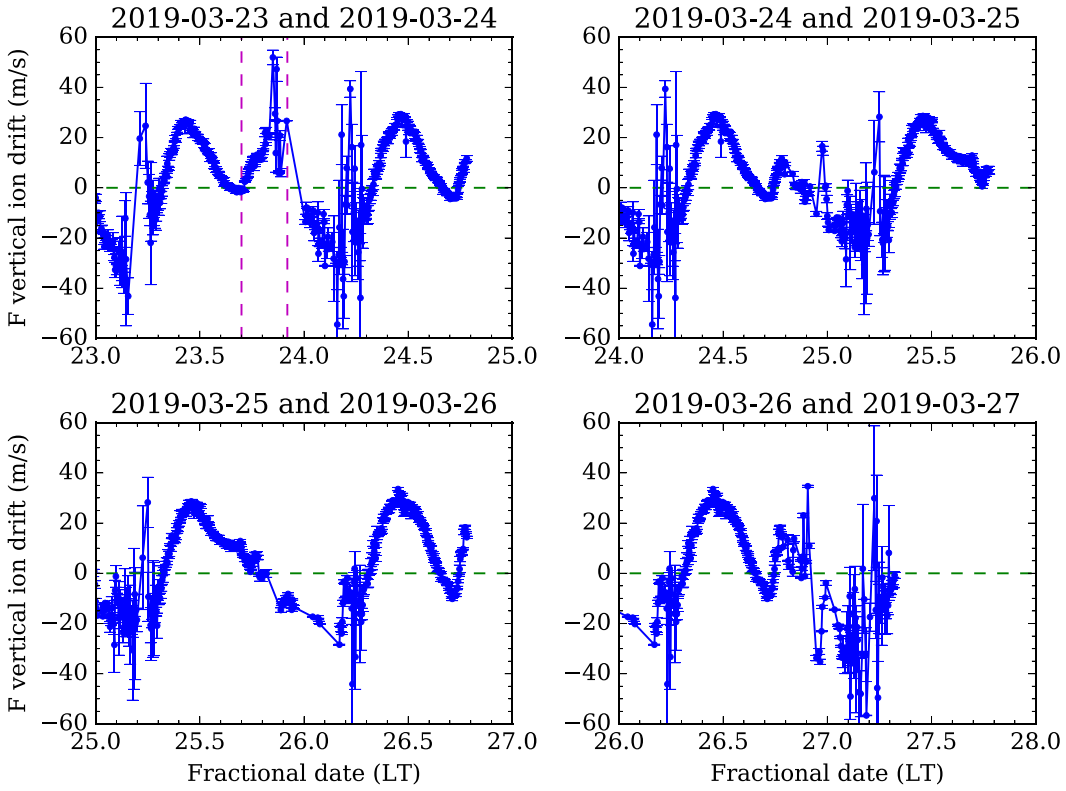

Figure 6. *F* region vertical ion drift from Jicamarca ISR during 5 days in March 2019. Interesting thing to note is that the *F* region drift is strongly upward over several hours, marked by dashes vertical lines, on the night of 23–24 March 2019. Jicamarca local time (LT = UT − 5 hr).

Americas is localized over central South American longitudes during the Northern Fall season. Also, the continuity of the EIA structures from premidnight sector as seen in Figure 5 implies that EM-EIA cannot be directly related to midlatitude arc or Weddell sea anomaly structures as reported in Zhang et al. (2013) and Chang et al. (2015).

4.3. What Causes the Localized Structures in EIA Over South America

As the electron production is nearly zero during nighttime, such persistent enhanced structure could be caused by wave dynamics or electro-dynamical processes or localized particle precipitation. For a qualitative investigation, we use about 5 days of *F* region vertical plasma drift measurements available during 23–27 March 2019 from Jicamarca incoherent scatter radar (ISR) in Peru, which are shown in Figure 6. During these 5 days (or 4 nights), the EM-EIA occurs over the Jicamarca longitude sector on 24 March 2019. The concurrent *F* region drift measurements and GOLD EM-EIA give us an opportunity to investigate the relationship between the vertical drifts and EM-EIA. It can be seen that on 23 March, the *F* region drift over Jicamarca was positive for about 5 hr (from roughly 1700–2200 LT hours, marked by vertical dashed lines). Under normal circumstances, prereversal enhancement (PRE) remains positive for about 1–2 hr (1800–2000) (Scherliess & Fejer, 1999), but on 23 March it was positive for about 5 hr, so we refer to this as an extended PRE event. Such extended PRE can lift the ambient *F* region plasma to very high altitudes, where chemical recombination or loss is small, allowing the plasma to persist for hours past midnight (Dao et al., 2011). The presence of significant TEC and early morning OI-135.6 nm nightglow around the Jicamarca longitudes, as can be seen in Figure 7, indeed indicates that in this case plasma uplift is a possible explanation for the early morning EIA in OI-135.6 nm emissions. There is another case where PRE lasted for about 3 hr on 26 March 2019, but OI-135.6 nm emission and TEC were not apparent in the early morning equatorial sector. This could be due to the relatively less enhanced and shorter duration PRE, at least as compared to the 23 March case. But due to the limited availability of concurrent vertical drift data, a definitive relationship between PRE and EM-EIA occurrence cannot be established. Future investigations using upcoming COSMIC-2 drift measurements (Yue et al., 2014) might enable us to establish a relationship

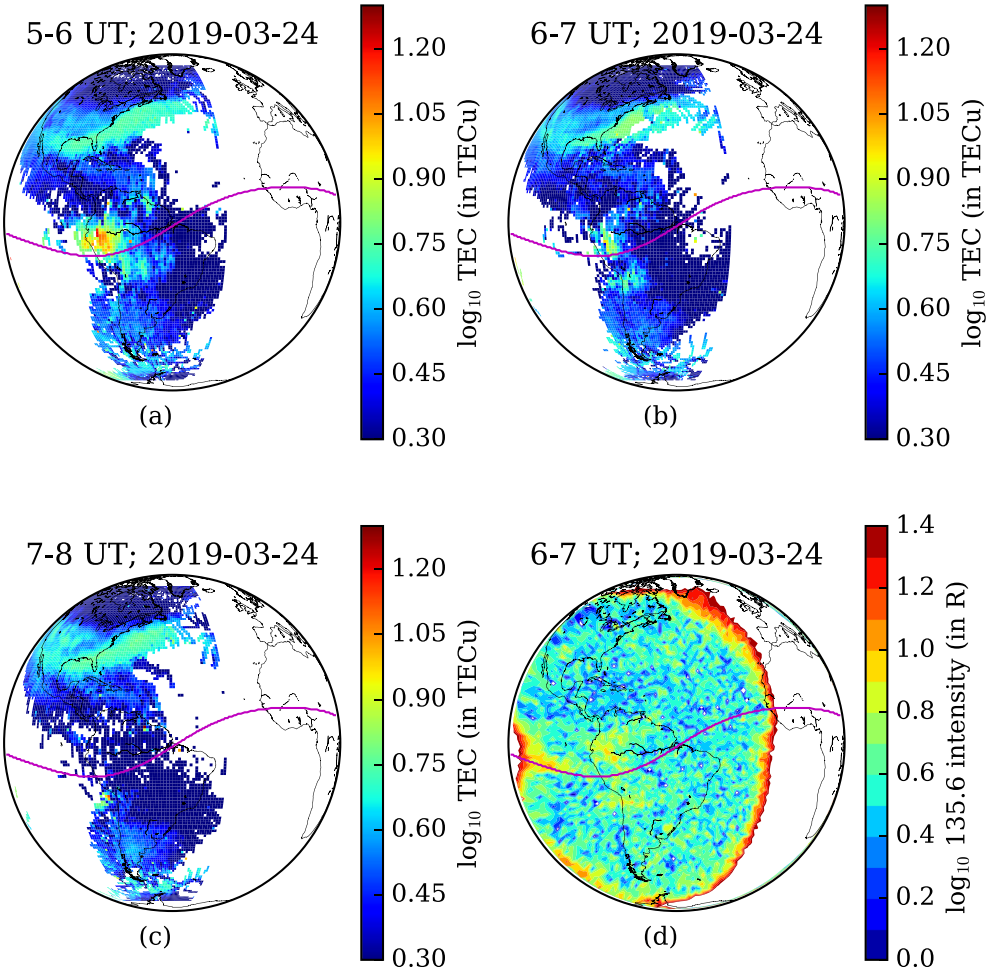

Figure 7. Same as Figure 4 but for 24 March 2019. Enhanced emission and TEC over Jicamarca longitudes can be seen, which is believed to be remains from premidnight lifted up plasma due to the strong and long lasting PRE. Though there are some highly fluctuating positive *F* region drifts between 3 and 5 LT on 24 March in Figure 6, the continuity of the TEC structures from previous night suggests that they are mainly the remnant.

between strength and duration of PRE and EM-EIA occurrence. Additionally, an equatorward meridional wind can also push the plasma upward along geomagnetic field lines (Valladares & Chau, 2012), which could help explain cases where the latitudinal distance between the crests are narrow, for example, the 24 October 2018 and 19 March 2019 cases as shown in Figure 1.

There are many cases of EM-EIA during October and November 2018, where Jicamarca drift measurements are also available, but the EM-EIA during these times occurred more than 10° eastward of Jicamarca, making it difficult to draw any conclusion about the relationship between vertical drift and EM-EIA. It should be noted that an enhanced and long-lasting PRE, as seen in the 23 March 2019 case, is not the only condition necessary for the occurrence of the EM-EIA, as it is also necessary that the electron density is sufficiently large during the afternoon and evening. Moreover, geomagnetic and solar wind conditions, as well as lower atmospheric dynamics, will also influence the PRE strength and duration and thus the occurrence of the EM-EIA (e.g., Batista et al., 2006).

The geomagnetic and solar activity conditions for majority of the days considered in this paper were quiet. For example, during 23–25 October 2019, hourly values of some indices were D_{st} index above −11 nT, F10.7 index below 71 sfu, solar wind speed below 360 km s^{-1}, IEF_y between 1.0 to −1.0 mV m^{-1}, and ap index was below 7 nT. For reference, a plot for these indices during the days of Figure 1 is given in Figure S1 in the supporting information. Very low values of these indices suggest that the enhancements seen above are

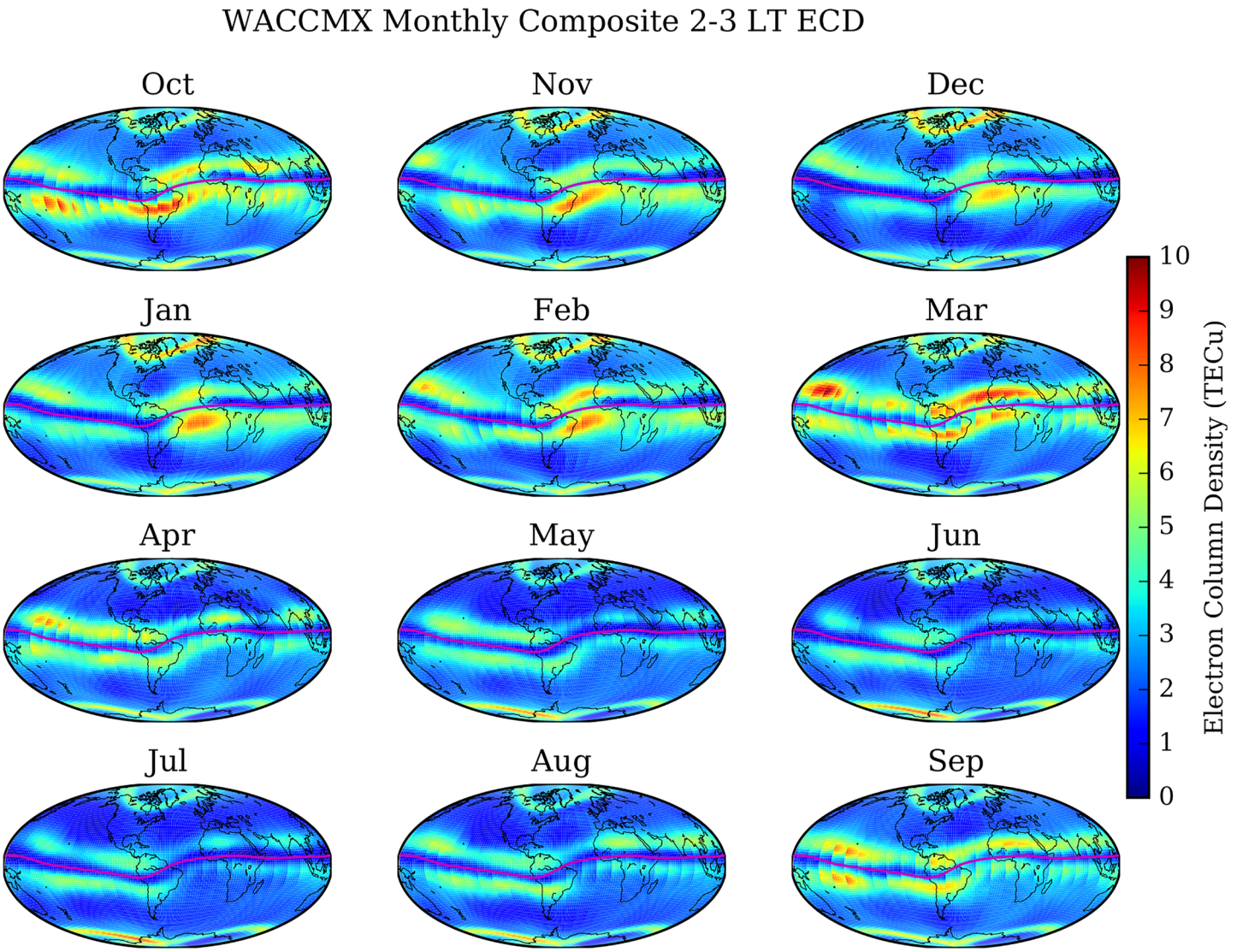

Figure 8. Monthly composite early morning (2–3 LT) WACCMX electron column density (ECD) values are presented. It shows that EM-EIA can be seen globally and it has a longitudinal Waves 4 or 3 pattern that changes its peak locations with season.

less likely related to geomagnetic or solar variability. Therefore, we propose that the enhanced and extended PRE is most likely due to wave-driven processes.

To investigate possible wave influences, we performed numerical simulations using WACCMX with constant solar minimum and quiet geomagnetic conditions. As the WACCMX simulations are free running, a particular day of the GOLD observations cannot be compared with a corresponding day in WACCMX, but the seasonal or monthly climatology can be. Figure 8 shows monthly composite WACCMX electron column density (ECD) for 2–3 LT. ECD is similar to TEC, but the column integration is up to the topmost layer of WACCMX, which is about 500 km for the current case. From the WACCMX ECD it is observed that the early morning EIA can occur globally and their occurrence show properties similar to ionospheric Wave 4 structure. For example, they are more prominent during equinoxes, shift their position with season, and are mostly asymmetric about the geomagnetic equator. These properties of EM-EIA suggest that their drivers are most likely the lower atmospheric DE3, SE2, and SPW4 waves (Pedatella et al., 2012), which can influence the PRE and thus the EIA (Fang et al., 2009). Fang et al. (2009) derived an ionospheric model with satellite-based PRE and were able to see the ionospheric Wave 4 structure in EIA, which they attributed to the influence of the DE3 tide. Their work and our results provide an explanation of the connnection between PRE, Wave 4 pattern, and EM-EIA.

The WACCMX ECD, in Figure 8, also helps to explain why the GOLD EM-EIA are not observed during solstices. This is because the EM-EIA local maximum over South America moves to the eastern side of the disk during northern winter and is too weak to be detected during northern Summer. The occasional longitudinally localized EM-EIA structure in GOLD, for example, in case of 23 October 2018, suggests that EM-EIA and its drivers can have significant day-to-day variability. This also suggest that GOLD disk observations are capable of detecting ionospheric day-to-day variability. Further investigations using multi-instrument global measurements and model simulations are needed to elucidate the mechanism that generates such localized EM-EIA structures. From the climatological behavior in the WACCMX one may also expect such occasional EM-EIA over Africa and Asia, particularly during equinoxes.

The localized EM-EIA structure in GOLD disk scans is observed to shift in longitude during different seasons. For example, they occur predominantly over the middle of South America during Fall (October–November) and in the western or Peruvian sector during Spring (March–April). This property of the localized feature also excludes the possibility that the enhanced OI-135.6 nm emission is due to electron precipitation through the South Atlantic anomaly and their subsequent transport to the equator through magnetic field lines.

5. Concluding Remarks

We have used about 10 months of GOLD OI-135.6 nm emission measurements to study the EM-EIA at synoptic scale and high-spatial resolutions. Day-to-day variability of EM-EIA shows that it can have occassional longitudinally localized crests. The seasonal and longitudinal variability of the EM-EIA over South America shows that it occurs during October–November over central South America and during March–April over western South America. In general, the northern spring time EM-EIA has less latitudinal extent compared to those during Northern Fall. Over the American landmass, the observed similarity between the OI 135.6 nm emissions and GNSS TEC demonstrates that the occurrence of the emission structures in the GOLD observations is due to radiative recombination.

Numerical simulations from WACCMX with constant solar minimum and quiet geomagnetic conditions show that EM-EIA can occur at other longitudes too and its seasonal variability has similar longitudinal shift as that of the GOLD EM-EIA over South America. Model results also show that EM-EIA has properties similar to ionospheric Wave 4 pattern, especially during equinoxes. This suggests that the drivers of EM-EIA are most likely linked to the lower atmosphere and point to DE3, SE2, and SPW4 waves. The occasional occurrence of very localized EM-EIA crests implies that early morning ionosphere can have significant day-to-day variability and GOLD disk measurements are capable of detecting them.

Data Availability Statement

Computing and data storage resources, including the Cheyenne supercomputer (doi:10.5065/D6RX99HX), were provided by the Computational and Information Systems Laboratory (CISL) at NCAR. The Level 1Cdata used in this study are available at the GOLD Science Data Center (https://gold.cs.ucf.edu/search/) and at NASA's Space Physics Data Facility (https://spdf.gsfc.nasa.gov/pub/data/gold/). GNSS TEC data productsand access through the Madrigal distributed data system are provided to the community (https://cedar.openmadrigal.org) by the Massachusetts Institute of Technology (MIT) under support from U.S. NationalScience Foundation Grant AGS-1242204.

Acknowledgments
This research was supported by NASA Contract 80GSFC18C0061 to the University of Colorado, Boulder. This material is also based upon work supported by the National Center for Atmospheric Research (NCAR), which is a major facility sponsored by the National Science Foundation under Cooperative Agreement 1852977.

References

Appleton, E. V. (1946). Two anomalies in the ionosphere. *Nature*, *157*(3995), 691–691. https://doi.org/10.1038/157691a0

Batista, I. S., Abdu, M. A., Souza, J. R., Bertoni, F., Matsuoka, M. T., Camargo, P. O., & Bailey, G. J. (2006). Unusual early morning development of the equatorial anomaly in the Brazilian sector during the Halloween magnetic storm. *Journal of Geophysical Research*, *111*, A05307. https://doi.org/10.1029/2005JA011428

Chang, L. C., Lin, C. H., Yue, J., Liu, J. Y., & Lin, J. T. (2013). Stationary planetary wave and nonmigrating tidal signatures in ionospheric Wave 3 and Wave 4 variations in 2007–2011 FORMOSAT-3/COSMIC observations. *Journal of Geophysical Research: Space Physics*, *118*, 6651–6665. https://doi.org/10.1002/jgra.50583

Chang, L. C., Liu, H., Miyoshi, Y., Chen, C. H., Chang, F. Y., Lin, C. H., et al. (2015). Structure and origins of the Weddell sea anomaly from tidal and planetary wave signatures in FORMOSAT-3/COSMIC observations and GAIA GCM simulations. *Journal of Geophysical Research: Space Physics*, *120*, 1325–1340. https://doi.org/10.1002/2014JA020752

Dao, E., Kelley, M. C., Roddy, P., Retterer, J., Ballenthin, J. O., de La Beaujardiere, O., & Su, Y. J. (2011). Longitudinal and seasonal dependence of nighttime equatorial plasma density irregularities during solar minimum detected on the C/NOFS satellite. *Geophysical Research Letters*, *38*, L10104. https://doi.org/10.1029/2011GL047046

Eastes, R. W., McClintock, W. E., Burns, A. G., Anderson, D. N., Andersson, L., Codrescu, M., et al. (2017). The Global-scale Observations of the Limb and Disk (GOLD) mission. *Space Science Reviews*, *212*(1-2), 383–408. https://doi.org/10.1007/s11214-017-0392-2

Eastes, R. W., Solomon, S. C., Daniell, R. E., Anderson, D. N., Burns, A. G., England, S. L., et al. (2019). Global-scale observations of the equatorial ionization anomaly. *Geophysical Research Letters*, *46*, 9318–9326. https://doi.org/10.1029/2019GL084199

England, S. L., Immel, T. J., Sagawa, E., Henderson, S. B., Hagan, M. E., Mende, S. B., et al. (2006). Effect of atmospheric tides on the morphology of the quiet time, postsunset equatorial ionospheric anomaly. *Journal of Geophysical Research*, *111*, A10519. https://doi.org/10.1029/2006JA011795

Fang, T. W., Kil, H., Millward, G., Richmond, A. D., Liu, J. Y., & Oh, S. J. (2009). Causal link of the Wave 4 structures in plasma density and vertical plasma drift in the low-latitude ionosphere. *Journal of Geophysical Research*, *114*, A10315. https://doi.org/10.1029/2009JA014460

Hanson, W. B. (1970). A comparison of the oxygen ion-ion neutralization and radiative recombination mechanisms for producing the ultraviolet nightglow. *Journal of Geophysical Research*, *75*(22), 4343–4346. https://doi.org/10.1029/JA075i022p04343

Heelis, R. A., Stoneback, R., Earle, G. D., Haaser, R. A., & Abdu, M. A. (2010). Medium-scale equatorial plasma irregularities observed by coupled ion-neutral dynamics investigation sensors aboard the communication navigation outage forecast system in a prolonged solar minimum. *Journal of Geophysical Research*, *115*, A10321. https://doi.org/10.1029/2010JA015596

Immel, T. J., Sagawa, E., England, S. L., Henderson, S. B., Hagan, M. E., Mende, S. B., et al. (2006). Control of equatorial ionospheric morphology by atmospheric tides. *Geophysical Research Letters*, *33*, L15108. https://doi.org/10.1029/2006GL026161

Laskar, F. I., Pallamraju, D., Lakshmi, T. V., Reddy, M. A., Pathan, B. M., & Chakrabarti, S. (2013). Investigations on vertical coupling of atmospheric regions using combined multiwavelength optical dayglow, magnetic, and radio measurements. *Journal of Geophysical Research: Space Physics*, *118*, 4618–4627. https://doi.org/10.1002/jgra.50426

Laskar, F. I., Pallamraju, D., & Veenadhari, B. (2014). Vertical coupling of atmospheres: Dependence on strength of sudden stratospheric warming and solar activity. *Earth Planets Space*, *66*(1), 94. https://doi.org/10.1186/1880-5981-66-94

Liu, H. L. (2016). Variability and predictability of the space environment as related to lower atmosphere forcing. *Space Weather*, *14*, 634–658. https://doi.org/10.1002/2016sw001450

Liu, H. L., Bardeen, C. G., Foster, B. T., Lauritzen, P., Liu, J., Lu, G., et al. (2018). Development and validation of the whole atmosphere community climate model with thermosphere and ionosphere extension (WACCM-X 2.0). *Journal of Advances in Modeling Earth Systems*, *10*, 381–402. https://doi.org/10.1002/2017MS001232

Liu, J., Liu, L., Zhao, B., Lei, J., & Wan, W. (2011). On the relationship between the postmidnight thermospheric equatorial mass anomaly and equatorial ionization anomaly under geomagnetic quiet conditions. *Journal of Geophysical Research*, *116*, A12312. https://doi.org/10.1029/2011JA016958

Liu, H. L., & Richmond, A. D. (2013). Attribution of ionospheric vertical plasma drift perturbations to large-scale waves and the dependence on solar activity. *Journal of Geophysical Research: Space Physics*, *118*, 2452–2465. https://doi.org/10.1002/jgra.50265

McDonald, S. E., Dymond, K. F., & Summers, M. E. (2008). Hemispheric asymmetries in the longitudinal structure of the low-latitude nighttime ionosphere. *Journal of Geophysical Research*, *113*, A08308. https://doi.org/10.1029/2007JA012876

Meléndez-Alvira, D. J., Meier, R. R., Picone, J. M., Feldman, P. D., & McLaughlin, B. M. (1999). Analysis of the oxygen nightglow measured by the Hopkins ultraviolet telescope: Implications for ionospheric partial radiative recombination rate coefficients. *Journal of Geophysical Research*, *104*(A7), 14,901–14,913. https://doi.org/10.1029/1999JA900136

Patra, A. K., & Phanikumar, D. V. (2009). Intriguing aspects of F-region plasma irregularities revealed by the Gadanki radar observations during the SAFAR campaign. *Annales Geophysicae*, *27*(10), 3781–3790. https://doi.org/10.5194/angeo-27-3781-2009

Pedatella, N. M., Hagan, M. E., & Maute, A. (2012). The comparative importance of DE3, SE2, and SPW4 on the generation of Wavenumber-4 longitude structures in the low-latitude ionosphere during September equinox. *Geophysical Research Letters*, *39*, L19108. https://doi.org/10.1029/2012GL053643

Qin, J., Makela, J. J., Kamalabadi, F., & Meier, R. R. (2015). Radiative transfer modeling of the OI 135.6 nm emission in the nighttime ionosphere. *Journal of Geophysical Research: Space Physics*, *120*, 10,116–10,135. https://doi.org/10.1002/2015JA021687

Retterer, J. M. (2005). Physics-based forecasts of equatorial radio scintillation for the Communication and Navigation Outage Forecasting System (C/NOFS). *Space Weather*, *3*, S12C03. https://doi.org/10.1029/2005sw000146

Rideout, W., & Coster, A. (2006). Automated GPS processing for global total electron content data. *GPS Solutions*, *10*(3), 219–228. https://doi.org/10.1007/s10291-006-0029-5

Rishbeth, H. (1997). The ionospheric E-layer and F-layer dynamos—A tutorial review. *Journal of Atmospheric and Solar-Terrestrial Physics*, *59*(15), 1873–1880. https://doi.org/10.1016/s1364-6826(97)00005-9

Rodrigues, F. S., Hickey, D. A., Zhan, W., Martinis, C. R., Fejer, B. G., Milla, M. A., & Arratia, J. F. (2018). Multi-instrumented observations of the equatorial F-region during June solstice: Large-scale wave structures and spread-F. *Progress in Earth and Planetary Science*, *5*, 16. https://doi.org/10.1186/s40645-018-0170-0

Scherliess, L., & Fejer, B. G. (1999). Radar and satellite global equatorial F region vertical drift model. *Journal of Geophysical Research*, *104*(A4), 6829–6842. https://doi.org/10.1029/1999JA900025

Sekar, R., Chakrabarty, D., Sarkhel, S., Patra, A. K., Devasia, C. V., & Kelley, M. C. (2007). Identification of active fossil bubbles based on coordinated VHF radar and airglow measurements. *Annales Geophysicae*, *25*(10), 2099–2102. https://doi.org/10.5194/angeo-25-2099-2007

Su, S. Y., Liu, C. H., Ho, H. H., & Chao, C. K. (2006). Distribution characteristics of topside ionospheric density irregularities: Equatorial versus midlatitude regions. *Journal of Geophysical Research*, *111*, A06305. https://doi.org/10.1029/2005JA011330

Tinsley, B. A., Christensen, A. B., Bittencourt, J., Gouveia, H., Angreji, P. D., & Takahashi, H. (1973). Excitation of oxygen permitted line emissions in the tropical nightglow. *Journal of Geophysical Research*, *78*(7), 1174–1186. https://doi.org/10.1029/JA078i007p01174

Valladares, C. E., & Chau, J. L. (2012). The low-latitude ionosphere sensor network: Initial results. *Radio Science*, *47*, RS0L17. https://doi.org/10.1029/2011rs004978

Vierinen, J., Coster, A. J., Rideout, W. C., Erickson, P. J., & Norberg, J. (2016). Statistical framework for estimating GNSS bias. *Atmospheric Measurement Techniques*, *9*(3), 1303–1312. https://doi.org/10.5194/amt-9-1303-2016

Yamazaki, Y., & Richmond, A. D. (2013). A theory of ionospheric response to upward-propagating tides: Electrodynamic effects and tidal mixing effects. *Journal of Geophysical Research: Space Physic*, *118*, 5891–5905. https://doi.org/10.1002/jgra.50487

Yizengaw, E., Moldwin, M. B., Sahai, Y., & de Jesus, R. (2009). Strong postmidnight equatorial ionospheric anomaly observations during magnetically quiet periods. *Journal of Geophysical Research*, *114*, A12308. https://doi.org/10.1029/2009JA014603

Yizengaw, E., Retterer, J., Pacheco, E. E., Roddy, P., Groves, K., Caton, R., & Baki, P. (2013). Postmidnight bubbles and scintillations in the quiet-time June solstice. *Geophysical Research Letters*, *40*, 5592–5597. https://doi.org/10.1002/2013GL058307

Yue, X., Schreiner, W. S., Pedatella, N., Anthes, R. A., Mannucci, A. J., Straus, P. R., & Liu, J. Y. (2014). Space weather observations by GNSS radio occultation: From FORMOSAT-3/COSMIC to FORMOSAT-7/COSMIC-2. *Space Weather*, *12*, 616–621. https://doi.org/10.1002/2014SW001133

Zhang, Y., Paxton, L. J., & Kil, H. (2013). Nightside midlatitude ionospheric arcs: TIMED/GUVI observations. *Journal of Geophysical Research: Space Physics*, *118*, 3584–3591. https://doi.org/10.1002/jgra.50327

Zhang, K., Wang, W., Wang, H., Dang, T., Liu, J., & Wu, Q. (2018). The longitudinal variations of upper thermospheric zonal winds observed by the champ satellite at low and midlatitudes. *Journal of Geophysical Research: Space Physics*, *123*, 9652–9668. https://doi.org/10.1029/2018JA025463

Zhong, J., Lei, J., Yue, X., Luan, X., & Dou, X. (2019). Middle-latitudinal band structure observed in the nighttime ionosphere. *Journal of Geophysical Research: Space Physics*, *124*, 5857–5873. https://doi.org/10.1029/2018JA026059